Greenhouse gases modulate the strength of millennial-scale subtropical rainfall, consistent with future predictions

Fei Guo[1,2,3*], Steven C. Clemens[3,*], Yuming Liu[2,4], Ting Wang[2,4], Huimin Fan[2], Xingxing Liu[2],

Youbin Sun[2,5,6]

[1]Institute of Marine Science and Technology, Shandong University, Qingdao 266237, China

[2]State Key Laboratory of Loess and Quaternary Geology, Institute of Earth Environment, Chinese Academy of Sciences, Xian 710061, China

[3]Department of Earth, Environmental, and Planetary Sciences, Brown University, Providence, RI 02912-1846, USA

[4]University of Chinese Academy of Sciences, Beijing 100049, China

[5]CAS Center for Excellence in Quaternary Science and Global Change, Xian 710061, China

[6]Open Studio for Oceanic-Continental Climate and Environment Changes, Pilot National Laboratory for Marine Science and Technology (Qingdao), Qingdao 266200, China

Corresponding author: Fei Guo (guofei@ieecas.cn) and Steven C. Clemens (steven_clemens@brown.edu)

Highlights

The new precipitation-sensitive proxy (Ca/Ti) shows persistent millennial-scale East Asian summer monsoon changes over past 650 ka;

The magnitude of millennial-scale variability is modulated by AMOC at the eccentricity and precession bands.

Increasing GHG and strong insolation lead to more frequent occurrence of extreme rainfall, consistent with model results.

Abstract: Millennial-scale East Asian monsoon variability is closely associated with natural hazards through long-term variability in flood and drought cycles. Therefore, exploring what drives the millennial-scale variability is of significant importance for future prediction of extreme climates. Here we present a new East Asian summer monsoon (EASM) rainfall reconstruction from the northwest Chinese loess plateau spanning the past 650 ka. The magnitude of millennial-scale variability (MMV) in EASM rainfall is linked to ice volume and greenhouse gas (GHG) at the 100-kyr earth-orbital eccentricity band and to GHG and summer insolation at the precession band. At the glacial-interglacial cycle, gradual changes in CO_2 at times of intermediate ice volume leads to increased variability in North Atlantic stratification and Atlantic meridional overturning circulation, propagating abrupt climate changes into East Asia via the westerlies. Within the 100-kyr cycle precession variability further enhances the response, showing that stronger insolation and increased atmospheric GHG cause increases in the MMV of EASM rainfall. These findings indicate increased extreme precipitation events under future warming scenarios, consistent with model results.

Key words: EASM rainfall, MMV, GHG modulation, precession band

1. Introduction

Chinese loess is a unique terrestrial archive that can well document East Asian monsoon (EAM) variability at tectonic to millennial timescales (Porter and An, 1995; An et al., 2011). High-resolution loess records have revealed persistent millennial-scale (1-10 kyr periodicity) EAM fluctuations spanning the last several glacial cycles (Guo et al., 1996; Sun et al., 2012, 2021a,b; Guo et al., 2021), which are dynamically linked with high-latitude abrupt changes in the

48   north Atlantic including Heinrich (H) (Heinrich, 1988) and Dansgaard-Oeschger (DO) events

49   (Dansgaard et al., 1982). This millennial-scale monsoon variability is superimposed on

50   glacial-interglacial variations (Ding et al., 1999; Clemens et al., 2018). Abrupt summer monsoon

51   changes are closely linked to natural hazards such as flood and drought events (Huang et al., 2007),

52   since the summer monsoon plays a leading role in transporting water vapor from low to

53   middle/high latitudes of the northern hemisphere (Liu et al., 2013; An et al., 2015). Abrupt rainfall

54   events associated with short-term summer monsoon variations strongly influence agriculture, food

55   production, water supply and social economic development (Huang et al., 2007; Cook et al., 2010;

56   Li et al., 2017). However, how these flood/drought events are affected by both natural and

57   anthropogenic factors remains poorly constrained. Understanding the mechanisms that modulate

58   the magnitude of millennial-scale variability (MMV) is of critical importance for the scientific

59   community as well as policy makers. Here we use the term "modulate" in the context of

60   lower-frequency components of the climate system influencing or determining the amplitude of a

61   higher-frequency components.

62   A number of well-dated, high-resolution speleothem $\delta^{18}O$ records have been developed in

63   recent years (Wang et al., 2008; Cheng et al., 2016), providing the opportunity to examine the

64   underlying relationship(s) between East Asian monsoon MMV and potential longer-term

65   (orbital-scale) modulators. The latest research suggests that the MMV through the Pleistocene is

66   influenced by both glacial boundary condition and orbital configurations (Sun et al., 2021b).

67   Cheng et al., (2016) hypothesized, on the basis of an East Asian composite speleothem $\delta^{18}O$

68   record ($\delta^{18}Osp$), that periods of maximum Northern Hemisphere summer insolation correspond to

69   weaker millennial-scale variability. Subsequently, however, Thirumalai et al (2020) showed that

70   precession does not modulate the MMV of $\delta^{18}O_{sp}$ and postulated that it is, instead, modulated by

71   internal processes related to the cryosphere. This work also raised the possibility that $\delta^{18}O_{sp}$ is

72   decoupled from regional Asian monsoon rainfall over millennial timescales (Zhang et al., 2018).

73   As such, two important outstanding questions remain; is there a reliable proxy for East Asian

74   summer monsoon (EASM) rainfall at the millennial timescale and what factors modulate the

75   MMV thereof?

76   Due to weak pedogenesis and high sedimentation rates, millennial-scale oscillations are well

77   preserved in the western and northwestern Chinese Loess Plateau (CLP) over the past glacial

78   cycles (Sun et al., 2012, 2021a; Guo et al., 2021). The Linxia profile is well-suited for

79   reconstructing rapid monsoon changes because it is located in monsoon frontal zone and sensitive

80   to high- and low-latitude climate variability. To address the above questions, we have generated a

81   high-resolution summer monsoon proxy (Ca/Ti) from Linxia on the western CLP (Fig. 1). The

82   Ca/Ti ratio is a precipitation-sensitive proxy linked to summer monsoon rainfall (Guo et al., 2021).

83   Low values of Ca/Ti indicate stronger Ca leaching associated with intensified summer rainfall.

84   The new precipitation proxy (Ca/Ti) and $\delta^{18}O_{sp}$ are evaluated to elucidate the modulating drivers

85   of these two proxy records. As discussed in the Results section, we find that the MMV of Ca/Ti is

86   mainly modulated by ice volume and greenhouse gases (GHG) at the eccentricity band. Both

87   GHG and summer insolation modulate the MMV of Ca/Ti at the precession band but not that of

88    $\delta^{18}O_{sp}$; $\delta^{18}O_{sp}$ MMV is modulated by winter insolation at the eccentricity and obliquity bands.

89   The interpretations of these results are presented in the Discussion section.

90   **2. Materials and Methods**

91   **2.1 Site and measurements of loess sections**

92   The Linxia (LX; 103.63°E, 35.15°N, 2,200 m a.s.l.) loess record is from the western edge of the

93   CLP (Fig. 1). At present, mean annual temperature and precipitation in this region are about 8.1°C

94   and 484 mm, respectively, with ~80% of the annual precipitation falling during the summer season

95   (May to September). The 203.8 m-long core A (LXA) consists of 185 m of eolian loess-paleosol

96   sequences, underlain by 17 m of fluvial loess and 1.8 m of sandy gravel layers. The 72 m-long

97   core B (LXB) and a 7 m pit were excavated in 2017. Powder samples were collected at 2 cm

98   intervals for analyzing mean grain size (MGS) with the resolution ranging 10~200 yr/cm. As well,

99   2-cm resolution samples were dried at 40°C overnight and ground to 200 mesh size (about <75

100   μm) with an agate mortar and pestle, and then pressed into a plastic sheet (4 cm × 4 cm × 0.3 cm),

101   creating a flat and homogeneous slide. The plastic slides were then placed on a wood pallet for

102   XRF scanning to obtain elemental intensities (Guo et al., 2021).

103   **2.2 Age model and evaluations of age uncertainties**

104   The chronological framework for Chinese loess-paleosol sequences is widely constructed by

105   matching grain-size to benthic LR04 $\delta^{18}O$ records (Porter and An, 1995; Hao et al., 2012; Sun et

106   al., 2021a). A similar approach utilizes correlation to speleothem $\delta^{18}O$ in recent years (Beck et al.,

107   2018; Sun et al., 2021a; Zhang et al., 2022). The age model of Linxia profile is generated by

108   synchronizing Chinese loess and speleothem $\delta^{18}O$ records back to 650 ka (published by Sun et al.,

109   in 2021a). Detailed information of loess/paleosol strata is showed in Fig. 2 and refers to Sun et

110   al.,(2021a). The first set of control points tie the loess/paleosol boundaries S_6 to S_0 to the timing of

111   the glacial terminations/inceptions in speleothem $\delta^{18}O$ (Cheng et al., 2016). The second and third

112   sets of age control points tie the timing of precessional transition boundaries and abrupt cooling

113   events in the MGS record to those in speleothem $\delta^{18}O$ (Fig. 2b), based on the assumption that the

114　East Asian summer and winter monsoon co-vary at orbital timescales, and millennial-scale abrupt

115　events are synchronous in the northern hemisphere (Hemming et al., 2004; Sun et al., 2012;

116　Clemens et al., 2018). The tie points are shown in Fig. 2b.

117　　The composite speleothem $\delta^{18}O$ record is well resolved by absolute U-Th dating and applied as

118　the target for regional synchronization. The errors are less than 2 kyr for the last 450 ka and

119　increase to 4-8 kyr before 450 ka (Cheng et al., 2019). The MGS record yields good correlation

120　between loess/paleosol boundaries and glacial/interglacial transitions of LR04 $\delta^{18}O$. The age

121　differences of most glacial terminations are around 2-4 kyr (Fig. 2b, Sun et al., 2021a) with

122　sedimentation rate ranging from 5-100 cm/kyr. The speleothem $\delta^{18}O$ synchronized age model is

123　compared with benthic $\delta^{18}O$ age model to evaluate the influence of age uncertainties on the

124　wavelet coherence analysis. The small differences in the two age models (correlation to marine

125　$\delta^{18}O$ and to speleothem $\delta^{18}O$) make little difference in the MMV and associated wavelet coherence

126　(WTC). This is because age model tie points are separated by 20-30 kyrs and the small differences

127　in the tie-points among the two age models has little to no influence on the amplitude (MMV) of

128　millennial-scale peaks. Only minor differences in the MMV WTC phase are observed at the

129　obliquity (450-550 ka) and precession bands (100-200 ka). (Compare Fig. S1 with Fig. 4).

130　**2.3 Spectrum and wavelet coherence analysis**

131　　In order to estimate the MMV, loess Ca/Ti and $\delta^{18}O_{sp}$ are linear interpolated at 0.1 kyr interval.

132　The WTC results remain unchanged unless the cutoff threshold is reduced to to 6 kyr or increased

133　it to 12 kyr; then original time series are filtered using a Butterworth filter at a cutoff threshold of

134　10 kyr (e.g. Ca/Ti-hi-10kyr). The moving standard deviation of millennial-scale variability is

135　calculated to ascertain the orbitally-related modulation and its association with internal and

136　external forcing using 2 kyr sliding window (calculation method follows Thirumalai et al., 2020).

137　The spectra of all proxies were calculated using the Lomb-Scargle periodogram

138　(https://exoplanetarchive.ipac.caltech.edu/cgi-bin/Pgram/nph-pgram), which has the advantage of

139　analyzing discontinuous time series and removal of spurious spectral characteristics (VanderPlas,

140　2018). Normalized and combined orbital parameters eccentricity, tilt, and negative precession

141　(ETP), GHG, insolation, and benthic $\delta^{18}O$ were evaluated by WTC to extract maximal phase and

142　amplitude correlations with astronomical, ice volume and greenhouse gases forcing over the past

143　650 ka. WTC between time series was performed in a Monte Carlo framework (n = 1, 000)

144　following Grinsted et al., (2004). The WTC would help to detect the period in different frequency

145　bands where the two time series co-vary (but does not necessarily have high power). The black

146　arrows in the figures represent the phrase relationship between the two time sequences with

147　rightward, upward and downward arrows indicate the in-phrase, leading and lagging phrase,

148　respectively. The colour scale indicates the amplitude correlations between the two datasets.

149　　In this paper, the parameter ΔRF_{GHG} is regarded as GHG radiative forcing (GHG RF, using the

150　GHG RF instead of ΔRF_{GHG} in the discussion section) and applied in WTC to evaluate the

151　relationship between MMV of Ca/Ti and $\delta^{18}O$ sp. The ΔRF_{GHG} is reconstructed by referencing the

152　content of EPICA ice core greenhouse gases to the modern value. ΔRF_{GHG} is defined as the

153　difference between a certain past GHG level ([CO_2] and [CH_4]) and the pre-industrial greenhouse

154　gas level ([CO_2]$_0$ = 280 ppm, [CH_4]$_0$ = 700 ppb) (Ramaswamy et al., 2001). While CH_4 contributes

155　<5%, we calculated the ΔRF_{GHG} using both CO_2 and CH_4. The equation used to determine ΔRF_{GHG}

156　is as follows (Lo et al., 2017):

157　　$\Delta RF_{GHG} = \Delta RF_{CO2} + \Delta RF_{CH4}$

158      $= 4.841\ln([CO_2]/[CO_2]_0) + 0.0906(\sqrt{[CO_2]} - \sqrt{[CO_2]_0}) + 0.036\ln(\sqrt{[CH_4]} - \sqrt{[CH_4]_0})$

159 **3. Results**

160   The MGS reflects grain-size sorting and is very sensitive to winter monsoon variations (Porter

161 and An, 1995; Sun et al., 2006) with larger particle size during the glacials. The Ca/Ti ratio

162 reflects precipitation-induced leaching intensity linked to summer monsoon rainfall (Guo et al.,

163 2021), with lower value during the interglacials. The high resolution δ^{18}O of Sanbao-Hulu

164 speleothem is an indicator of EASM changes at orbital to centennial timescales (Cheng et al.,

165 2016). The MGS and Ca/Ti exhibit distinct glacial-interglacial and precessional variations over the

166 last 650 ka as seen in LR04 δ^{18}O (Lisiecki and Raymo, 2005) and speleothem δ^{18}O (Cheng et al.,

167 2016), respectively (Fig. 2b).

168   Both Ca/Ti and δ^{18}Osp records show clear millennial-scale fluctuations overlaying orbital-scale

169 variations. The high frequency millennial signals (Materials and Methods) persist over the last 650

170 ka, but the amplitude varies from proxy to proxy (Fig. 3a and S2a). Spectral analysis of the raw

171 records and MMV for loess and speleothem records display variable associations with

172 eccentricity- (~100 kyr), obliquity- (~41 kyr), and precession-scale (~23 and ~19 kyr) over the

173 past 650 ka. Loess Ca/Ti variance is mainly concentrated in obliquity with lesser variance in the

174 eccentricity and precession bands (Fig. 3b), indicating prominent ice volume (eccentricity and

175 obliquity) and isolation (precession) forcing. The speleothem δ^{18}O shows predominant

176 precession-scale variance (Fig. S2b) suggesting strong links to insolation forcing (Cheng et al.,

177 2016). These results indicate ice volume and insolation play dominant roles in driving changes in

178 loess Ca/Ti and speleothem δ^{18}O, respectively (Cheng et al., 2016; Sun et al., 2021a).

179   Millennial-scale fluctuations co-exist with long-term orbital- and ice-volume variability; we

180   seek to assess the potential linkages among them and in particular, the extent to which MMV is

181   modulated by these longer-term orbital and internal climate parameters. The spectra of Ca/Ti

182   MMV shows dominant eccentricity with less strong precession and weak obliquity variance (Fig.

183   3d). The spectrum of $\delta^{18}O$sp MMV has a small peak near 100 kyr and an offset 41 kyr peak with

184   little to no variance at the 23 kyr period (Fig. S2d). Thus, while both proxies are similarly

185   modulated at the 100-kyr period (such that the MMV is larger during glacial intervals relative to

186   interglacial times) the MMV modulation is variable for the two proxies at other orbital bands.

187   As with the spectral differences in the raw records, the MMV spectra also implies different

188   MMV modulating drivers, potentially associations with insolation, ice volume, and/or GHG

189   (Thirumalai et al., 2020). How do internal and external drivers interact with each other and

190   modulate the MMV of these records at the orbital timescale? We performed wavelet coherence

191   and phase analyses of both MMV records relative to ETP, ice volume, ΔRF_{GHG}, summer insolation,

192   and winter insolation to identify which variables might modulate the MMV of these EASM

193   records. The MMV in Ca/Ti is strongly coherent with ice volume and GHG at the 100,000-year

194   earth-orbital eccentricity band and with GHG and summer insolation at the 23,000-year precession

195   band (Fig. 4c, d, g). $\delta^{18}O$sp MMV is most strongly coherent with GHG and ice volume at the

196   100-kyr band and with winter insolation at the eccentricity and obliquity bands (Fig. S3c, d, g).

197   **4. Discussion**

198   **4.1 Orbital-scale modulation factors for MMV of the EASM**

199   Previous geological records and modeling indicate that high latitude ice volume or ice sheet

200   topography play important roles in triggering abrupt climate changes (Broecker et al.,1994; Clark

201   et al., 2001). In particular, abrupt climate changes are highly sensitive to ice volume variations; ice

202   sheets are widely hypothesized to motivate and amplify these high frequency signals within a

203   constrained benthic oxygen isotope-"ice volume threshold" between 3.5 and 4.5‰ (Bailey et al.,

204   2010; Naffs et al., 2013; Zhang et al., 2014). Wavelet coherence between the MMV of loess Ca/Ti,

205   speleothem $\delta^{18}O$ and the global benthic $\delta^{18}O$ stack show excellent coherence and near-zero phase

206   with ice volume at the 100 kyr band (Fig. 4e, g and S3e, g); this in-phase variation demonstrates

207   that EASM MMV primarily follows the glacial-interglacial rhythm of ice volume variations,

208   enlarged during glacial times and dampened during interglacial times. However, coherence of the

209   MMV for these two proxies with the benthic $\delta^{18}O$ stack is relatively weak and variable at the 41

210   kyr band ($\delta^{18}O$sp; Fig. S3e, g) and 23-kyr band (Ca/Ti; Fig. 4e, g). These relationships

211   demonstrate that ice volume directly modulates the MMV of the EASM, predominantly at the 100

212   kyr band, with high ice volume corresponding to larger MMV.

213   GHG concentration is another potential driver of abrupt climate changes (Alvarez-Solas et al.,

214   2011; Zhang et al., 2017).Wavelet coherence between the MMV of loess Ca/Ti, speleothem $\delta^{18}O$

215   and the record of GHG RF show excellent coherence and ~180° phase at the 100-kyr eccentricity

216   band (Fig. 4b, d and S3b, d) indicating strong MMV at times of low GHG. Given the coupled

217   nature of global ice-volume and atmospheric GHG, it is clear that over the late Pleistocene

218   glacial-interglacial cycles, these two factors modulate the MMV of the EASM as recorded by

219   Ca/Ti and speleothem $\delta^{18}O$ such that abrupt climate change is amplified during times of high ice

220   volume and low GHG concentration. However, this is not the case for the precession band. MMV

221   of loess Ca/Ti displays discrete intervals high coherence and near-zero phase with GHG RF at the

222   precession band (Fig. 4b, d), which is not the case for speleothem $\delta^{18}O$ (Fig. S3b, d). Thus, GHG

223   RF does play a role in modulating Ca/Ti MMV but not that of $\delta^{18}O$sp at the precession band,

224   indicating a difference in the millennial-scale response of these two proxies at this time-scale. We

225   investigate this further by assessing the response to local insolation forcing.

226   The MMV of Ca/Ti show discontinuous relatively weak coherence with 35°N summer

227   insolation at the precession band with even weaker coherence at the 41-kyr band (Fig. 4a, c); we

228   note that the summer insolation modulation is less strong relative to that of GHG at the precession

229   band (Fig. 4b, d). In contrast, the MMV of $\delta^{18}O_{sp}$ displays high coherence and zero phase with

230   35°N winter insolation at 100 kyr period, relatively weaker coherence, with a lagging phase, at the

231   41 kyr band, and negligible coherence at the 23-ky band (Fig. S3a, c). These results indicate that

232   the MMV of speleothem $\delta^{18}O$ is modulated by local winter insolation, opposite to the Cheng et al.,

233   (2016) hypothesis calling on north hemisphere summer insolation.

234   **4.2 Mechanism and implication for modulation of EASM MMV**

235   At the glacial-interglacial timescale, the MMV is amplified under the glacial boundary

236   conditions. This indicates dynamic linkages with high latitude North Atlantic Heinrich and DO

237   events (Cheng et al., 2016; Sun et al., 2012, 2021a, b). Heinrich and DO variability are linked to

238   Northern Hemisphere ice sheet (NHIS) perturbations via its influence on fresh-water flux into the

239   North Atlantic Ocean and consequent Atlantic meridional overturning circulation (AMOC)

240   changes (McManus et al., 1999; Hemming, 2004; Naffs et al., 2013). At times of intermediate ice

241   sheet volume, minor changes in NHIS height and atmospheric CO_2 concentrations can trigger the

242   rapid climate transitions (Zhang et al., 2014, 2017). Altering the height of NHIS leads to changes

243   in the gyre circulation and sea-ice coverage by shifting the northern westerlies (Zhang et al., 2014).

244   The maximum westerly wind stress shifts northwards associated with gradual increase of the

245   Northern Hemisphere ice volume. The northward westerly, in turn, encourages the EASM rain belt

246   to move northward (He et al., 2021) and results in increases in the MMV of EASM rainfall

247   (especially northern China). In addition, CO_2 acts as an internal feedback agent to AMOC changes

248   (Barker et al., 2016). Under intermediate glacial condition, when the AMOC reaches a regime of

249   bi-stability, rising CO_2 during Heinrich Stadial cold events can trigger abrupt transitions to warm

250   conditions. Decreasing CO_2 during warm events leads to abrupt cooling transitions (Zhang et al.,

251   2017). Therefore, CO_2 generally provides a negative feedback on MMV of EASM rainfall. During

252   interglacial times decreasing ice volume, accompanied by reduced sea ice and more frequent

253   freshwater perturbation, is correlated with lower frequency and smaller amplitude variability in

254   abrupt climate events. The co-evolving GHG concentrations would further alter the sea surface

255   temperature by greenhouse forcing, subsequently modulating the MMV.

256   Within the 100,000-year cycle, precession-band variability (4-5 cycles), characterized by

257   increased insolation and atmospheric GHG, further heightens the positive response, leading to

258   larger MMV of subtropical rainfall. Recent transient sensitivity experiments suggests that

259   millennial-scale rainfall variability is driven primarily by meltwater and secondarily by insolation

260   (He et al., 2021). During interglacial times under the combined influence of insolation and CO_2,

261   model simulation shows that when insolation reaches the lower "threshold" value (between 358.2

262   and 352.1 W. m^{-2}), it triggers a strong abrupt weakening of the AMOC and results in abrupt

263   cooling transitions over last 800 ka (Yin et al., 2021). Increased insolation could warm sea surface

264   temperature and accelerate freshwater input from high latitude ice sheet as well as altering GHG

265   concentration in the atmosphere (Lewkowicz and Way, 2019), which could, in turn, modulate

266   MMV changes in the low latitude monsoon regions.

267   If both millennial-scale Ca/Ti and $\delta^{18}Osp$ represent subtropical rainfall amount, the

268   modulation factors should be consistent. However, eccentricity, obliquity and precession bands

269   MMV modulators differ for loess Ca/Ti and $\delta^{18}Osp$, indicating they monitor different aspects of

270   millennial-scale monsoon circulations. Modern observations and Lagrangian trajectories of air

271   parcels in China during the summer monsoon indicate that moisture-induced precipitation doesn't

272   derive from the strongest water vapor pathways (Sun et al., 2011; Jiang et al., 2017); local water

273   vapor recycling contributes significantly to regional precipitation in East China (over 30%) and

274   North China (exceeding 55%) (Shi et al., 2020). Hence, we speculate that $\delta^{18}Osp$ MMV monitors

275   changes in the isotopic composition of rainfall, varying with changes in westerly transport paths

276   associated with North Atlantic cooling events, consistent with the MMV of $\delta^{18}Osp$ being closely

277   linked to winter insolation at 100- and 41- kyr periods and the absence of MMV modulation at

278   precession band. We further hypothesize that Ca/Ti mainly represents the MMV in local rainfall

279   amount, consistent with the MMV of tropical rainfall being more dynamically related to GHG and

280   summer insolation at precession band.

281   In recent decades atmospheric GHG concentration is accelerating due to anthropogenic

282   contribution of fossil fuels, suggesting that EASM (extreme) precipitation will increase as well.

283   This inference is consistent with model simulations indicating that the number of extreme daily

284   precipitation events and mean precipitation overall will increase significantly in response to higher

285   GHG concentration (Dairaku and Emori, 2006). The anthropogenic GHG-evoked warming is

286   projected to increase the lower-tropospheric water vapor content and enhance the thermal contrast

287   between land and ocean (Kitoh et al., 1997). This will give rise to a northward shift of lower

288   tropospheric monsoon circulation and an increase rainfall during the East Asian summer monsoon

289   (Vecchi and Soden, 2007). Our results indicate that factors modulating EASM precipitation MMV

in the past are consistent with those predicted to influence future changes in monsoonal precipitation, lending further confidence in those projections.

5. Conclusions

Our high-resolution loess Ca/Ti record displays millennial monsoon oscillations that persist over the last 650 ka. Wavelet results highlight remarkable GHG modulation at both 100 kyr and precession band as well as ice volume at 100 kyr period and local insolation forcing at precession band. The MMV of loess Ca/Ti and speleothem $\delta^{18}O$ are modulated by different orbital factors, implying that these two proxies document different climatic response of millennial-scale monsoon circulation. The inferred mechanism of how these internal and external factors modulate the MMV calls on dynamic linkages to variability in AMOC at both eccentricity and precession bands. In recent decades, atmospheric GHG concentration is dramatically increasing due to anthropogenic contribution of fossil fuels (Bousquet et al., 2006; Davis et al., 2010), resulting in accelerated melting of ice-sheets in bi-polar regions (Swingedouw et al., 2008; Golledge et al., 2019). Their combined effects lead to more frequent occurrences of extreme rainfall (Dairaku and Emori, 2006; IPCC, 2018). Our results indicate that the MMV EASM rainfall is modulated by ice volume, GHG, and insolation factors, consistent with those predicted to influence future changes in monsoonal precipitation.

Declaration of Competing Interest

The authors declare that they have no known competing financial interests or personal relationships that could have appeared to influence the work reported in this paper.

References

Alvarez-Solas, J., Charbit, S., Ramstein, G., Paillard, D., Dumas, C., Ritz, C., and Roche, D. M.: Millennial-scale oscillations in the Southern Ocean in response to atmospheric CO_2 increase, Global Planet. Change, 76, 128-136, https://doi.org/10.1016/j.gloplacha.2010.12.004, 2011.

An, Z., Clemens, S. C., Shen, J., Qiang, X., Jin, Z., Sun, Y., Prell, W. L., Luo, J., Wang, S., Xu, H., Cai, Y., Zhou, W., Liu, X., Liu, W., Shi, Z., Yan, L., Xiao, X., Chang, H., Wu, F., Ai., L., and Lu, F.: Glacial-interglacial Indian summer monsoon dynamics, Science, 333, 719-723, https://doi.org/10.1126/science.1203752, 2011.

An, Z., Wu, G., Li, L., Li, J., Sun, Y., Liu, Y., Zhou, W., Cai, Y., Duan, A., Li, L., Mao, J., Cheng, H., Shi, Z., Tan, L., Yan, H., Ao, H., Chang, H., and Feng, J.: Global monsoon dynamics and climate change, Annu. Rev. Earth Planet., 43, 29-77, https://doi.org/10.1146/annurev-earth-060313-054623, 2015.

Bailey, I., Bolton, C. T., DeConto, R. M., Pollard, D., Schiebel, R., and Wilson, P. A.: A low threshold for North Atlantic ice rafting from "low-slung slippery" late Pliocene ice sheets, Paleoceanography, 25, PA1212, https://doi.org/10.1029/2009PA001736, 2010.

Barker, S., and Knorr, G.: A paleo-perspective on the AMOC as a tipping element, PAGES News,

339   24, 14-15, http://orca.cardiff.ac.uk/id/eprint/95186, 2016.

340   Beck, J. W., Zhou, W., Li, C., Wu, Z., White, L., Xian, F., Kong, X., and An, Z. A 550,000-year

341   record of East Asian monsoon rainfall from [10]Be in loess. Science, 360, 877-881,

342   https://www.science.org/doi/abs/10.1126/science.aam5825, 2018.

343   Bousquet, P., Ciais, P., Miller, J. B., Dlugokencky, E. J., Hauglustaine, D. A., Prigent, C., and

344   White, J.: Contribution of anthropogenic and natural sources to atmospheric methane variability,

345   Nature, 443, 439-443, https://doi.org/10.1038/nature05132, 2006.

346   Broecker, W. S.: Massive iceberg discharges as triggers for global climate change, Nature, 372

347   421-424, https://doi.org/10.1038/372421a0, 1994.

348   Cheng, H., Edwards, L., Sinha, A., Spötl, C., Yi, L., Chen, S., Kelly, M., Kathayat, G., Wang, X. F.,

349   Li, X. L., Kong, X. G., Wang, Y. J., Ning, Y.F., and Zhang, H. W.: The Asian monsoon over the

350   past 640,000 years and ice age terminations, Nature, 534, 640-646,

351   https://doi.org/10.1038/nature18591, 2016.

352   Clark, P. U., Marshall, S. J., Clarke, G. K., Hostetler, S. W., Licciardi, J. M., and Teller, J. T.:

353   Freshwater forcing of abrupt climate change during the last glaciation, Science, 293, 283-287,

354   https://doi.org/10.1126/science.1062517, 2001.

355   Clemens, S. C., Holbourn, A., Kubota, Y., Lee, K. E., Liu, Z., Chen, G., Nelson, A., and

356   Fox-Kemper, B.: Precession-band variance missing from East Asian monsoon runoff, Nat.

357   Commun., 9, 1-12, https://doi.org/10.1038/s41467-018-05814-0, 2018.

358   Cook, E. R., Anchukaitis, K. J., Buckley, B. M., D'Arrigo, R. D., Jacoby, G. C., and Wright, W. E.:

359   Asian monsoon failure and megadrought during the last millennium, Science, 328, 486-489,

360   https://doi.org/10.1126/science.1185188, 2010.

361   Dansgaard, W., Clausen, H. B., Gundestrup, N., Hammer, C. U., Johnsen, S. F., Kristinsdottir, P.

362   M., and Reeh, N.: A new Greenland deep ice core, Science, 218, 1273-1277,

363   https://doi.org/10.1126/science.218.4579.1273, 1982.

364   Dairaku, K., and Emori, S.: Dynamic and thermodynamic influences on intensified daily rainfall

365   during the Asian summer monsoon under doubled atmospheric CO_2 conditions, Geophys. Res.

366   Lett., 33, L01704, https://doi.org/10.1029/2005GL024754, 2006.

367   Davis, S. J., Caldeira, K., and Matthews, H. D.: Future CO_2 emissions and climate change from

368   existing energy infrastructure, Science, 329, 1330-1333,

369   https://doi.org/10.1126/science.1188566, 2010.

370   Golledge, N. R., Keller, E. D., Gomez, N., Naughten, K. A., Bernales, J., Trusel, L. D., and

371   Edwards, T. L.: Global environmental consequences of twenty-first-century ice-sheet melt,

372   Nature, 566, 65-72, https://doi.org/10.1038/s41586-019-0889-9, 2019.

373   Grinsted, A., Moore, J. C., and Jevrejeva, S.: Application of the cross wavelet transform and

374   wavelet coherence to geophysical time series, Nonlinear Proc. Geoph., 11, 561-566,

375   https://doi.org/10.5194/npg-11-561-2004, 2004.

376   Guo, F., Clemens, S. C., Wang, T., Wang, Y., Liu, Y., Wu, F., Jin, Z., and Sun, Y.: Monsoon

377   variations inferred from high-resolution geochemical records of the Linxia loess/paleosol

378   sequence, western Chinese Loess Plateau, Catena, 198, 105019,

379   https://doi.org/10.1016/j.catena.2020.105019, 2021.

380   Guo, Z., Liu, T., Guiot, J., Wu, N., Lü, H., Han, J., and Gu, Z.: High frequency pulses of East

381   Asian monsoon climate in the last two glaciations: link with the North Atlantic. Clim. Dynam,

382   12, 701-709, https://doi.org/10.1007/s003820050137, 1996.

383   He, C., Liu, Z., Otto-Bliesner, B. L., Brady, E. C., Zhu, C., Tomas, R., Clark, P. U., Zhu, J., Jahn,

384   A., Gu, S., and Zhang, J., Nusbaumer, J., Noone, D., Cheng, H., Wang, Y., Yan, M., and Bao, Y.:

385   Hydroclimate footprint of pan-Asian monsoon water isotope during the last deglaciation, Sci.

386   Adv., 7, eabe2611, https://doi.org/10.1126/sciadv.abe2611, 2021.

387   Heinrich, H.: Origin and consequences of cyclic ice rafting in the northeast Atlantic Ocean during

388   the past 130,000 years, Quat. Res., 29, 142-152, https://doi.org/10.1016/0033-5894(88)90057-9,

389   1988.

390   Hemming, S. R.: Heinrich events: Massive late Pleistocene detritus layers of the North Atlantic

391   and their global climate imprint, Rev. Geophys., 42, RG1005,

392   https://doi.org/10.1029/2003RG000128, 2004.

393   Hoegh-Guldberg, O., Jacob, D., and Bindi, M., et al.: Impacts of 1.5 C global warming on natural

394   and human systems. Global warming of 1.5 C, An IPCC Special Report. IPCC Secretariat,

395   175-311, http://hdl.handle.net/10138/311749, 2018.

396   Huang, R., Chen, J., and Huang, G.: Characteristics and variations of the East Asian monsoon

system and its impacts on climate disasters in China, Adv. Atmos. Sci., 24, 993-1023, https://doi.org/10.1007/s00376-007-0993-x, 2007.

Jiang, Z., Jiang, S., Shi, Y., Liu, Z., Li, W., and Li, L.: Impact of moisture source variation on decadal-scale changes of precipitation in North China from 1951 to 2010, Geophys. Res. Atmos., 122, 600-613, https://doi.org/10.1002/2016JD025795, 2017.

Kitoh, A., Yukimoto, S., Noda, A., and Motoi, T.: Simulated changes in the Asian summer monsoon at times of increased atmospheric CO_2, J.Meteorol. Soc. JPN. Ser. II, 75, 1019-1031, https://doi.org/10.2151/jmsj1965.75.6_1019, 1997.

Lai, Z. P., and Wintle, A. G.: Locating the boundary between the Pleistocene and the Holocene in Chinese loess using luminescence, Holocene 16, 893-899, https://doi.org/10.1191/0959683606hol980rr, 2006.

Lewkowicz, A. G., and Way, R. G.: Extremes of summer climate trigger thousands of thermokarst landslides in a High Arctic environment, Nat. Commun., 10, 1-11, https://doi.org/10.1038/s41467-019-09314-7, 2019.

Lisiecki, L. E., and Raymo, M. E.: A Pliocene-Pleistocene stack of 57 globally distributed benthic $\delta^{18}O$ records, Paleoceanography, 20, PA1003, https://doi.org/10.1029/2004PA001071, 2005.

Liu, J., Wang, B., Cane, M. A., Yim, S. Y., and Lee, J. Y.: Divergent global precipitation changes induced by natural versus anthropogenic forcing, Nature, 493, 656-659, https://doi.org/10.1038/nature11784, 2013.

Lo, L., Chang, S. P., Wei, K. Y., Lee, S. Y., Ou, T. H., and Chen, Y. C., et al.: Nonlinear climatic sensitivity to greenhouse gases over past 4 glacial/interglacial cycles, Sci. Rep., 7, 1-7, https://doi.org/10.1038/s41598-017-04031-x, 2017.

McManus, J. F., Oppo, D. W., and Cullen, J. L.: A 0.5-million-year record of millennial-scale climate variability in the North Atlantic, Science, 283, 971-975, https://doi.org/10.1126/science.283.5404.971, 1999.

Naafs, B. D. A., Hefter, J., and Stein, R.: Millennial-scale ice rafting events and Hudson Strait Heinrich (-like) Events during the late Pliocene and Pleistocene: a review, Quat. Sci. Rev., 80, 1-28, https://doi.org/10.1016/j.quascirev.2013.08.014, 2013.

Porter, S. C., and An Z. S.: Correlation between climate events in the North Atlantic and China

during the last glaciation, Nature, 375, 305-308, https://doi.org/10.1038/375305a0, 1995.

Ramaswamy, V. et al.: Radiative forcing of climate change in Climate Change 2001: The Scientific Basis, Cambridge University Press, 349-416, https://csl.noaa.gov/assessments/ozone/1991/chapters/chapter7.pdf, 2001.

Shi, Y., Jiang, Z., Liu, Z., and Li, L.: A Lagrangian analysis of water vapor sources and pathways for precipitation in East China in different stages of the East Asian summer monsoon, J. Clim., 33, 977-992, https://doi.org/10.1175/JCLI-D-19-0089.1, 2020.

Sun, B., Zhu, Y., and Wang, H.: The recent interdecadal and interannual variation of water vapor transport over eastern China, Adv. Atmos. Sci., 28, 1039-1048, https://doi.org/10.1007/s00376-010-0093-1, 2011.

Sun, Y., Clemens, S. C., An, Z., and Yu, Z.: Astronomical timescale and palaeoclimatic implication of stacked 3.6-Myr monsoon records from the Chinese Loess Plateau, Quat. Sci. Rev., 25, 33-48. https://doi.org/10.1016/j.quascirev.2005.07.005, 2006.

Sun, Y., Clemens, S., Guo, F., Liu, X., Wang, Y., Yan, Y., and Liang, L.: High-sedimentation-rate loess records: A new window into understanding orbital-and millennial-scale monsoon variability, Earth-Sci. Rev., 103731, https://doi.org/10.1016/j.earscirev.2021.103731, 2021a.

Sun, Y., Clemens, S. C., Morrill, C., Lin, X., Wang, X., and An, Z.: Influence of Atlantic meridional overturning circulation on the East Asian winter monsoon, Nat. Geosci., 5, 46-49, https://doi.org/10.1038/ngeo1326, 2012.

Sun, Y., McManus, J. F., Clemens, S. C., Zhang, X., Vogel, H., Hodell, D. A., Guo, F., Wang, T., Liu, X., and An, Z.: Persistent orbital influence on millennial climate variability through the Pleistocene, Nat. Geosci., 14, 812-818, https://doi.org/10.1038/s41561-021-00794-1, 2021b.

Swingedouw, D., Fichefet, T., Huybrechts, P., Goosse, H., Driesschaert, E., and Loutre, M. F.: Antarctic ice-sheet melting provides negative feedbacks on future climate warming, Geophys. Res. Lett., 35, https://doi.org/10.1029/2008GL034410, 2008.

Thirumalai, K., Clemens, S. C., and Partin, J. W.: Methane, Monsoons, and Modulation of Millennial-Scale Climate, Geophys. Res. Lett., 47, e2020GL087613, https://doi.org/10.1029/2020GL087613, 2020.

Vecchi, G. A., and Soden, B. J.: Global warming and the weakening of the tropical circulation, J.

455   Clim., 20, 4316-4340, https://doi.org/10.1175/JCLI4258.1, 2007.

456   VanderPlas, J. T.: Understanding the lomb-scargle periodogram, The Astrophysical Journal

457   Supplement Series, 236, 16, https://doi.org/10.3847/1538-4365/aab766, 2018.

458   Wang, Y., Cheng, H., Edwards, R. L., Kong, X., Shao, X., Chen, S., and An, Z. Millennial-and

459   orbital-scale changes in the East Asian monsoon over the past 224,000 years, Nature, 451,

460   1090-1093, https://doi.org/10.1038/nature06692, 2008.

461   Yin, Q. Z., Wu, Z. P., Berger, A., Goosse, H., Hodell, D.: Insolation triggered abrupt weakening of

462   Atlantic   circulation   at   the   end   of   interglacials,   Science,   373,   1035-1040,

463   https://doi.org/10.1126/science.abg1737, 2021.

464   Zhang, H., Griffiths, M. L., Chiang, J.C.H., Kong, W., Wu, S., Atwood, A., Huang, J., Cheng, H.,

465   Ning, Y., and Xie, S.: East Asian hydroclimate modulated by the position of the westerlies

466   during Termination I, Science, 362, 580-583, https://doi.org/10.1126/science.aat9393, 2018.

467   Zhang, X., Knorr, G., Lohmann, G., and Barker, S.: Abrupt North Atlantic circulation changes in

468   response to gradual CO_2 forcing in a glacial climate state, Nat. Geosci., 10, 518-523,

469   https://doi.org/10.1038/ngeo2974, 2017.

470   Zhang, X., Lohmann, G., Knorr, G., and Purcell, C.: Abrupt glacial climate shifts controlled by ice

471   sheet changes, Nature, 512, 290-294, https://doi.org/10.1038/nature13592, 2014.

472   Zhang, Z., Li, G., Cai, Y., Cheng, X., Sun, Y., Zhao, J., Shu, P., Ma, L., and An, Z. Millennial‐

473   Scale Monsoon Variability Modulated by Low‐Latitude Insolation During the Last Glaciation.

474   Geophys. Res. Lett., 49, e2021GL096773, https://doi.org/10.1029/2021GL096773, 2022.

475

476
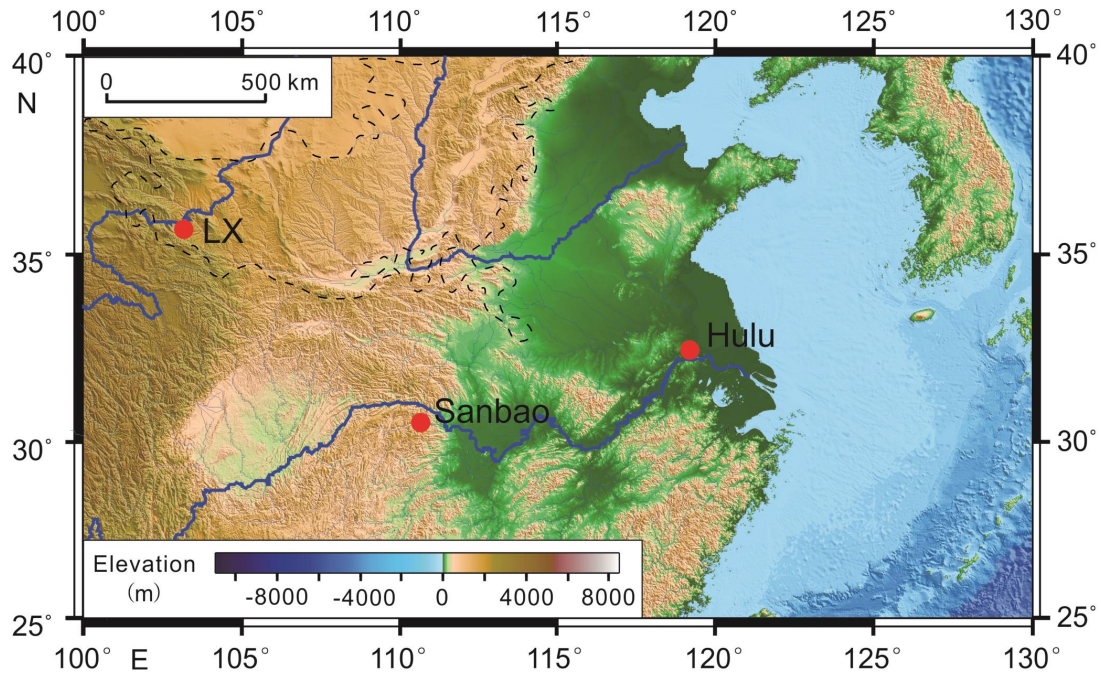
Figure. 1 The location of the Linxia (LX) loess profile and Hulu-Sanbao cave records. The Linxia

profile, located on the edge of convergence zone for of alpine Qinghai-Tibet Plateau, northwest

arid and the southeast monsoon area, is very sensitive to the migration of desert regions and

monsoonal rainfall. Sanbao-Hulu cave is located in monsoon-influenced Yangtze River Valley,

sensitive to the monsoon-induced precipitation changes. Black dash line represents the scope of

Chinese Loess Plateau. The base map is drawn using GMT software, and the elevation data is

from http://www.ngdc.noaa.gov/mgg/global/global.html.

484
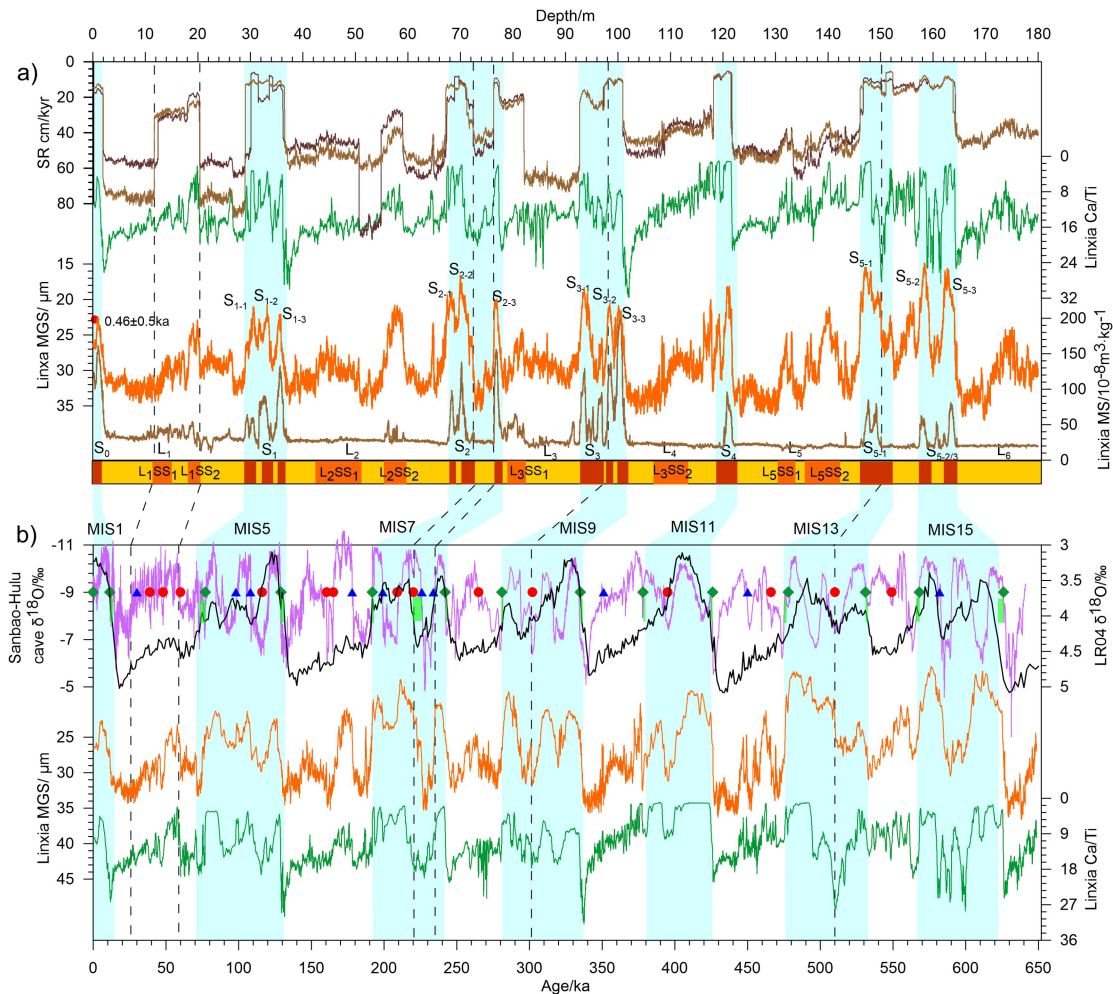
Figure 2 a) Strata and down-core variations of mean grain size (MGS), magnetic susceptibility (MS), Ca/Ti and sedimentation rate against depth (brown in benthic $\delta^{18}O$ age model and dark brown in speleothem $\delta^{18}O$ age model). Brown red, orange and yellow rectangles represent palaeosol layers, weakly pedogenic palaeosol in loess layers and loess layers, respectively. The timing of dash lines and glacial-interglacial transition are control points of benthic $\delta^{18}O$ chronology; b) Variations of MGS, Ca/Ti over last 650 ka and age model of Linxia loess section. Comparison of MGS and Ca/Ti in Linxia section with Sanbao-Hulu (Cheng et al., 2009, 2016) and benthic $\delta^{18}O$ stack (Lisiecki and Raymo, 2005). The dark brown squares, blue triangles and red dots represent the first (glacial-interglacial transition), second (precession cycles) and third (millennial-scale events) class age control points at the corresponding position of cave record, respectively (Sun et al., 2021a). Light blue bands donate the interglacial times. The short green rectangles represent the age differences between the two age models.

22
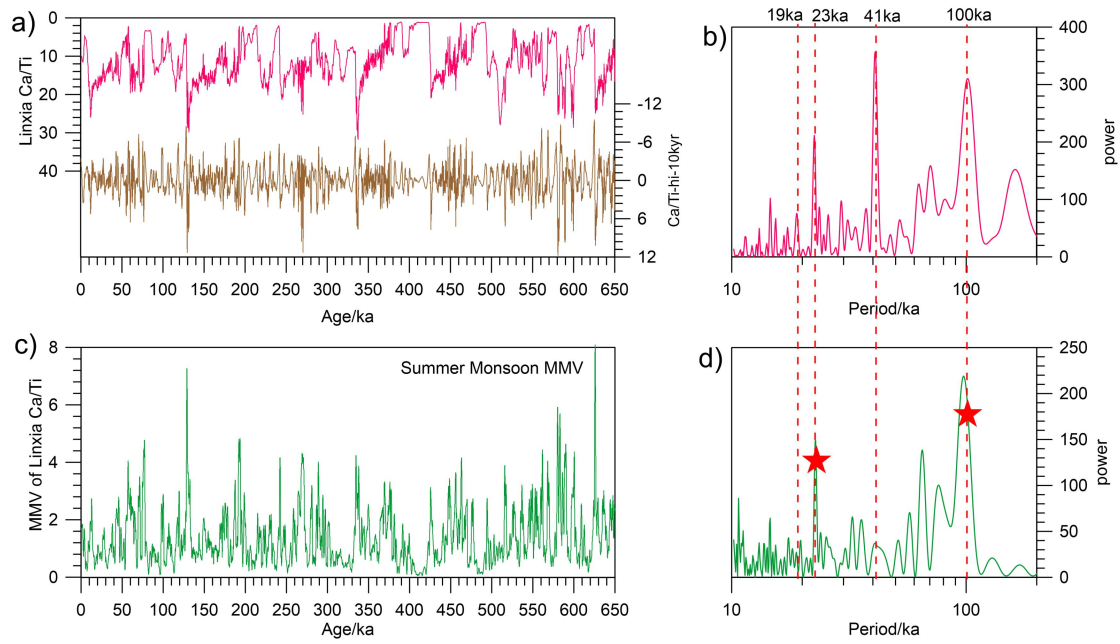
Figure. 3 Raw datasets, millennial-scale components (10 kyr high pass filtering signals) and MMV of the Linxia loess Ca/Ti record over the past 650 ka with their corresponding spectra. The orbital bands are marked with red dashed lines (eccentricity-100 kyr, obliquity-41 kyr ,precession-23 kyr and 19 kyr). Clearly variable eccentricity, obliquity and precession variances as well as persistent millennial-scale components are observed for loess Ca/Ti and MMV.
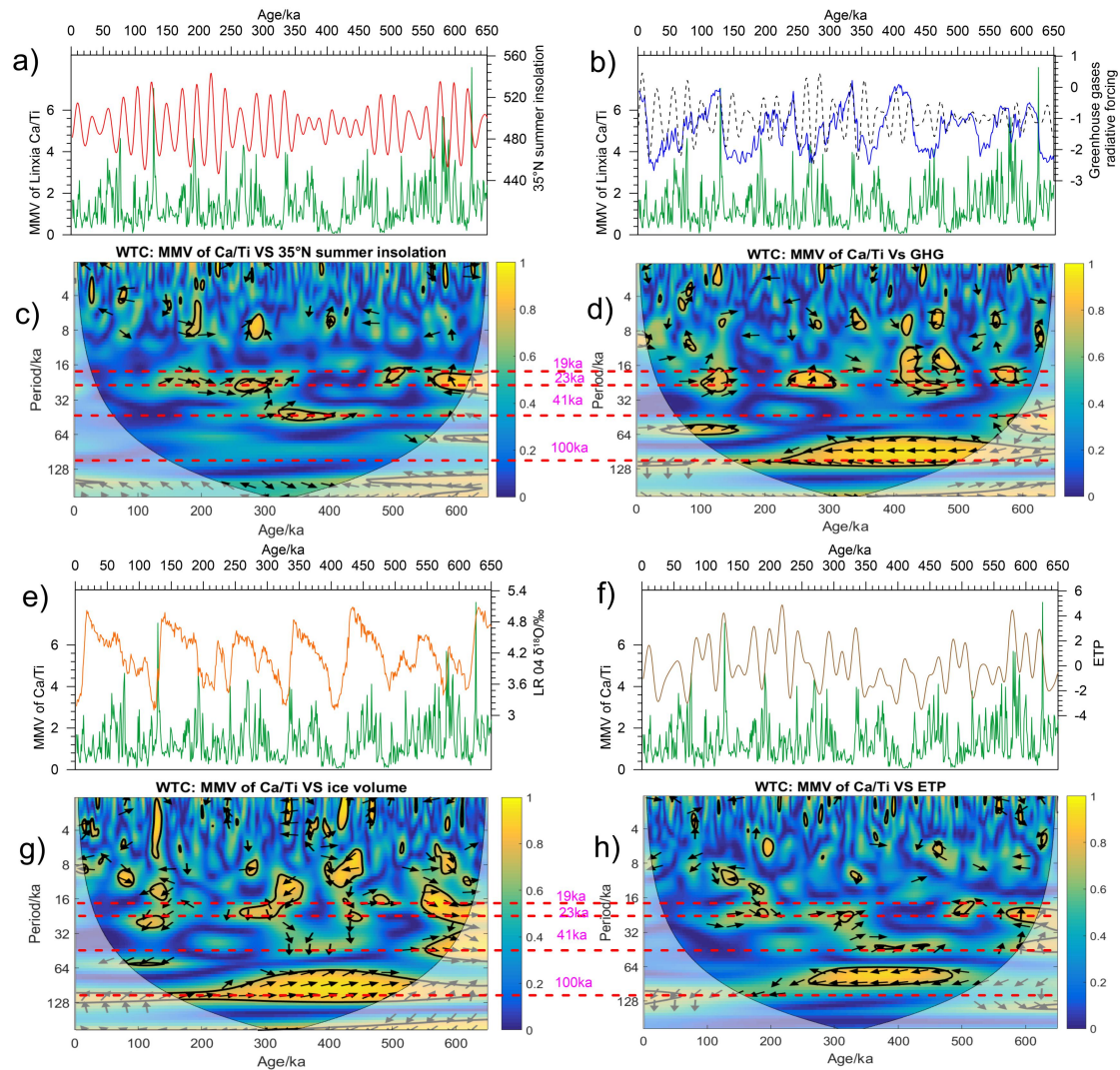
Figure. 4 Comparison of a) 35°N summer insolation forcing, b) GHG radiative forcing (black dish line donates the precession band-pass filtering results of ΔRF_GHG) and e) ice volume and f) ETP for MMV of Linxia loess Ca/Ti; Wavelet coherence between c) 35°N summer insolation, d) GHG radiative forcing, g) ice volume, h) ETP and MMV of loess Ca/Ti over the past 650 ka. The orbital bands are marked with red dashed lines (eccentricity-100 kyr, obliquity-41 kyr , precession-23 kyr and 19 kyr). The orange color indicates strong correlation for the two time series. The black lines plot coefficients of determination is more than 0.76. The black arrows represent the phrase relationship with rightward, upward and downward arrows indicating in-phrase, leading and lagging phrase, respectively. Strong eccentricity, weak obliquity and precession bands ice volume modulation are observed for MMV of loess Ca/Ti. Strong eccentricity and precession bands GHG modulation as well as weak summer insolation forcing are detected for MMV of loess Ca/Ti.